Dynamics and instabilities of defects in two-dimensional crystals on curved backgrounds

Mark Bowick,[1] Homin Shin,[1] and Alex Travesset[2]
[1]*Department of Physics, Syracuse University, Syracuse, New York 13244-1130, USA*
[2]*Ames Laboratory and Department of Physics and Astronomy, Iowa State University, Ames, Iowa 50011, USA*
(Received 31 October 2006; published 22 February 2007; corrected 27 February 2007)

Point defects are ubiquitous in two-dimensional crystals and play a fundamental role in determining their mechanical and thermodynamical properties. When crystals are formed on a curved background, finite-length grain boundaries (scars) are generally needed to stabilize the crystal. We provide a continuum elasticity analysis of defect dynamics in curved crystals. By exploiting the fact that any point defect can be obtained as an appropriate combination of disclinations, we provide an analytical determination of the elastic spring constants of dislocations within scars and compare them with existing experimental measurements from optical microscopy. We further show that vacancies and interstitials, which are stable defects in flat crystals, are generally unstable in curved geometries. This observation explains why vacancies or interstitials are never found in equilibrium spherical crystals. We finish with some further implications for experiments and future theoretical work.

DOI: 10.1103/PhysRevE.75.021404 PACS number(s): 82.70.Dd, 61.72.Bb, 61.72.Ji, 61.72.Mm

I. INTRODUCTION

The rich physics of the ordering of matter on planar surfaces takes on a new complexion when the ordering occurs on a curved two-dimensional manifold. Gaussian curvature, for example, favors the appearance of topological defects that are energetically prohibitive in planar systems. This has been demonstrated in the case of sufficiently large spherical crystals [1–6], toroidal hexatics [7], and both crystals and hexatics draped over a Gaussian bump [8,9].

For the simplest case of crystalline order on the constant-curvature two-sphere (the surface of a solid ball in R^3) the key new feature is the appearance of scars (Fig. 1), linear strings of dislocations around a central disclination that freely terminate inside the crystal, for crystals with radius above a microscopic-potential-dependent critical radius [1–3]. Scars have been observed experimentally in systems of colloidal beads self-adsorbed on spherical water droplets in an oil emulsion [10]. The imaging technique (conventional microscopy) in these experiments only allowed spherical caps covering 10%–20% of the full sphere to be imaged. Recently the use of fluorescently labeled colloidal particles and laser scanning confocal microscopy allowed the imaging of 50% of the sphere. In this way the global spatial distribution of scars was also measured [11].

Recent experiments [12,13] have investigated the dynamics of defects by directly visualizing colloidal particles absorbed on spherical oil-water interfaces. It was shown that dislocation glide within the scars (see Fig. 2) could be described very accurately by a harmonic potential binding the dislocation to the scar and an empirical Peierls potential that models the underlying crystalline lattice. The spring constants of the harmonic potentials, the elastic stiffness of the dislocation, were obtained from fits to the experimental results. In this paper, we show that continuum elasticity theory [1,2] can be used to provide explicit first-principles predictions for the elastic stiffness.

Defects such as vacancies and interstitials are quite common in two-dimensional crystals [14]. It has been shown that, quite generally, the presence of vacancies and interstitials significantly reduces the crystal's strength as a result of stress enhancement effects [15]. Jain and Nelson [16] performed an extensive investigation of interstitials and vacancies in two-dimensional planar crystals and identified three different interstitials and vacancies, depending on their symmetry, as the prevalent structures. Subsequent experiments [17] confirmed the stability of these defects and studied their dynamics. Very recently, Brownian dynamics simulations [18] have revealed a complex kinetics with a variety of

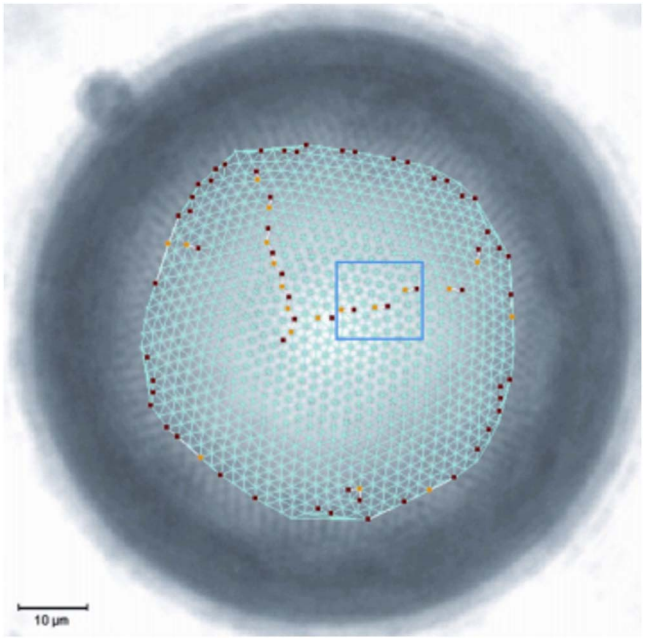

FIG. 1. (Color online) A light microscope image, reproduced from [12], of a water droplet with an 85 μm diameter and 1.9 μm mean particle spacing ($R/a \approx 22$). Fivefold (+1) disclinations are colored red, sevenfold (−1) disclinations are colored yellow, and tightly bound five to seven pairs represent dislocations. The three dislocations whose dynamics are analyzed in this paper are displayed within the blue box.

 ©2007 The American Physical Society

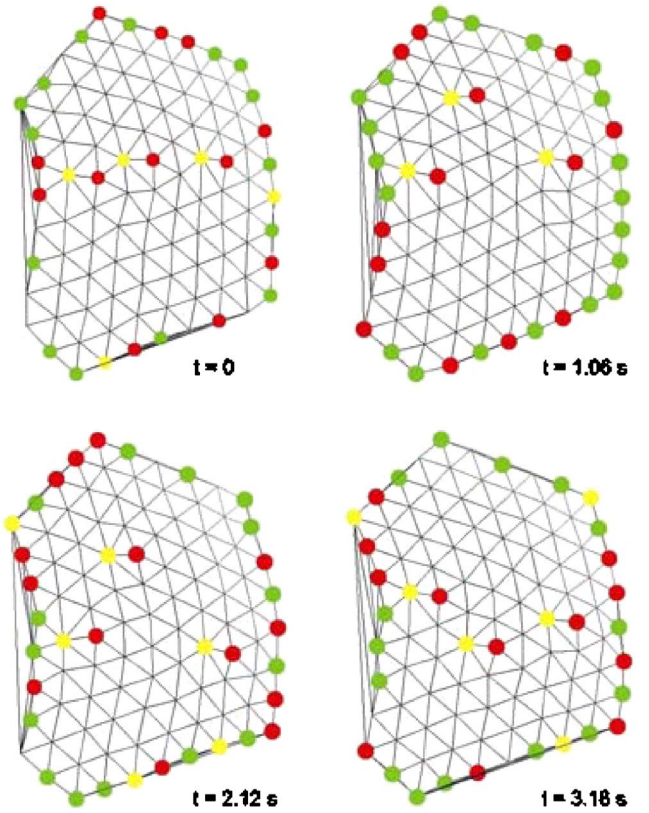

FIG. 2. (Color online) The dynamics of the three dislocations within the blue box of Fig. 1 taken from Ref. [12]. Motion consists of local Brownian fluctuation about the equilibrium position together with larger-scale glide.

modes that allow defects to glide and rotate. Rather interestingly, vacancies and interstitials have not been observed either experimentally or in numerical simulations [19] in spherical crystals. In this paper, we provide a study of the stability of vacancies and interstitials in curved two-dimensional crystals. Our analysis uses continuum theory, and therefore the results are directly applicable to other systems such as, for example, the analysis of vacancies and their relation to failure stress, which has recently investigated in straight carbon nanotubes [20], which provides another example for curved crystals.

The paper is organized as follows: In Sec. II we describe the dynamics of scar defects and the continuum elasticity theory of defect interactions. The theoretical results so obtained are compared to the experiment in Sec. III. In Sec. IV we study the instability of interstitials and vacancies in curved crystals with the continuum elastic model. The Thomson problem java applet used for this analysis is described in the Appendix.

II. DYNAMICS OF SCAR DEFECTS

A. Empirical description of scar dynamics

The scar dynamics is obtained from light microscopy as discussed in Ref. [12]. A typical snapshot of a configuration is shown in Fig. 1 and its evolution as a function of time is

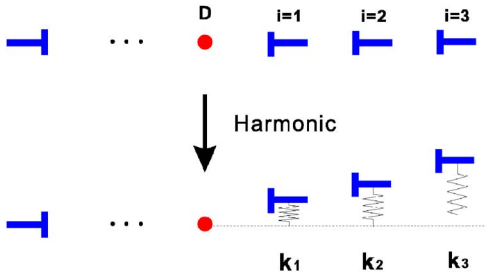

FIG. 3. (Color online) Spring model of dislocation binding. The red dot (D) represents the central disclination, and the blue sticks ($i=1,2,\ldots$) represent successive dislocations emanating from the central disclination. The spring constants $k_1,k_2,\ldots$ represent the binding of each dislocation to its parent scar.

shown in Fig. 2, showing some dislocations within the scar gliding at different times. In Ref. [12], it was shown that these data are well described by a model where each dislocation within the scar is pinned by a harmonic potential with spring constant k_i (here i labels the position of the dislocation within the scar) as shown in Fig. 3—that is,

$$U_i^{tot} = \frac{1}{2}k_i s_i^2 - U_0 \cos(2\pi s_i/a), \tag{1}$$

where s_i is the geodesic displacement of the ith dislocation on the surface of a sphere and the last term is the Peierls potential [21], which models the underlying crystalline structure of the lattice. Values for the experimentally determined spring constants were determined in Ref. [12]. We now provide the details leading to an explicit evaluation for the elastic stiffness.

B. Continuum elasticity of scars in curved backgrounds

We first present a discussion of the elasticity of scars. Point topological defects can be parametrized by disclinations. We therefore introduce a disclination density

$$Q(\mathbf{x}) = \frac{\pi}{3\sqrt{g(\mathbf{x})}}\sum_{i=1}^{N} q_i \delta(\mathbf{x}-\mathbf{x}_i), \tag{2}$$

where q_i is the disclination charge ($q_i=+1$ for 5's and -1 for 7's). The elastic energy of an arbitrary disclination density has been discussed extensively [1–3] and is given by

$$E = \frac{Y}{2}\int\int d^2\mathbf{x}d^2\mathbf{y}\sqrt{g(\mathbf{x})}\sqrt{g(\mathbf{y})}[K(\mathbf{x})-Q(\mathbf{x})]\left.\frac{1}{\Delta^2}\right|_{\mathbf{xy}} \times[K(\mathbf{y})-Q(\mathbf{y})] + NE_c, \tag{3}$$

where $K(x)$ is the Gaussian curvature of the background with metric $g(\mathbf{x})$, Y is the two-dimensional Young's modulus, and E_c is the disclination core energy. Both Y and E_c depend on the microscopic particle potential.

The free energy of Eq. (3) for a spherical crystal with the disclination density of Eq. (2) is then [1–3]

$$E = \frac{\pi Y}{36} R^2 \sum_{i=1}^{N} \sum_{i>j}^{N} q_i q_j \chi(\theta_i, \phi_i; \theta_j, \phi_j) + N E_c, \tag{4}$$

where

$$\chi(\beta) = 1 + \int_0^{(1-\cos\beta)/2} dz \frac{\ln z}{1-z} \tag{5}$$

and β is the angular geodesic length between points (θ_i, ϕ_i) and (θ_j, ϕ_j):

$$\cos\beta = \cos\theta_i \cos\theta_j + \sin\theta_i \sin\theta_j \cos(\phi_i - \phi_j). \tag{6}$$

The previous energy is a function of disclinations only. It is convenient to introduce dislocations explicitly. A dislocation can be regarded as a tightly bound disclination dipole, leading to a defect density

$$Q(\mathbf{x}) = \frac{\pi}{3\sqrt{g(\mathbf{x})}} \sum_{i=1}^{N_1} q_i \delta(\mathbf{x} - \mathbf{x}_i) + \frac{1}{\sqrt{g(\mathbf{x})}} \sum_{j=1}^{N_2} b^j_\alpha \epsilon_{\alpha\beta} \partial^j_\beta \delta(\mathbf{x} - \mathbf{x}_j). \tag{7}$$

As discussed elsewhere [1–3] the number of disclinations, N_1, is determined by the Euler characteristic χ of the background $N_1 = 6\chi$, thus giving 12 for the sphere. We also note that the Burgers vector $\vec{b}$ is perpendicular to the dipole direction defined by the vector connecting the two disclinations forming the dislocation. The elastic energy, Eq. (4), includes now a disclination-dislocation energy E_{Dd} and a dislocation-dislocation energy E_{dd} given by

$$\begin{aligned} E_{Dd} &= Y \int\int d^2\mathbf{x} d^2\mathbf{y} \frac{\pi}{3} \sum_{i=1}^{N_1} q_i \delta(\mathbf{x} - \mathbf{x}_i) \left. \frac{1}{\Delta^2} \right|_{\mathbf{xy}} \\ &\times \sum_{j=1}^{N_2} b^j_\alpha \epsilon_{\alpha\beta} \partial^j_\beta \delta(\mathbf{y} - \mathbf{y}_j) \\ &= \frac{YR^2}{12} \sum_{i=1}^{N_1} \sum_{j=1}^{N_2} q_i b^j_\alpha \epsilon_{\alpha\beta} \partial^j_\beta \chi(\theta_i, \phi_i; \theta_j, \phi_j) \end{aligned} \tag{8}$$

and

$$\begin{aligned} E_{dd} &= Y \int\int d^2\mathbf{x} d^2\mathbf{y} \sum_{i=1}^{N_2} b^i_\alpha \epsilon_{\alpha\beta} \partial^i_\beta \delta(\mathbf{x} - \mathbf{x}_i) \left. \frac{1}{\Delta^2} \right|_{\mathbf{xy}} \\ &\times \sum_{i>j}^{N_2} b^j_\gamma \epsilon_{\gamma\delta} \partial^j_\delta \delta(\mathbf{y} - \mathbf{y}_j) \\ &= \frac{YR^2}{4\pi} \sum_{i=1}^{N_2} \sum_{i>j}^{N_2} [b^i_\alpha \epsilon_{\alpha\beta} \partial^i_\beta][b^j_\gamma \epsilon_{\gamma\delta} \partial^j_\delta] \chi(\theta_i, \phi_i; \theta_j, \phi_j). \end{aligned} \tag{9}$$

In spherical coordinates, we have $b^i_\alpha \epsilon_{\alpha\beta} \partial^i_\beta = b^i_\theta \partial^i_\phi - b^i_\phi \partial^i_\theta$. We assume that both components of the angular Burgers vector, b^i_θ and b^i_ϕ, are approximately $|\vec{b}^i|/R$, where $|\vec{b}^i|$ is taken to be the lattice spacing a. An explicit expression for the energy of an arbitrary dislocation distribution interacting with N_1 disclinations is provided by combining Eqs. (8) and (9).

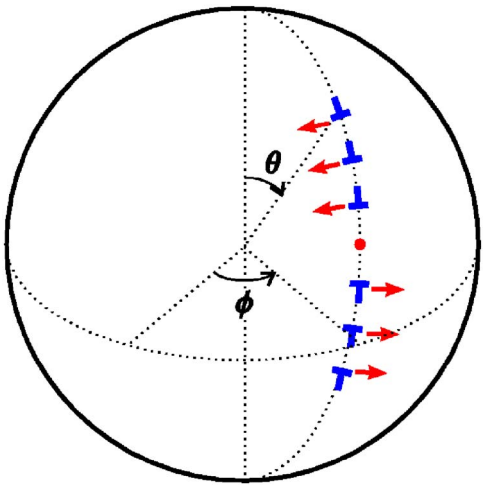

FIG. 4. (Color online) Schematic diagram of a single scar aligned along a geodesic meridian on the two-sphere. The red arrows indicate the associated Burgers vector for each dislocation.

Let us consider geodesically straight scars, symmetric about their midpoint and aligned along the fixed-ϕ meridian, as shown in Fig. 4. With this choice Eq. (6) gives $\phi_i = \phi_j$ and $\cos\beta = \cos(\theta_i - \theta_j)$. The Burgers vectors $\vec{b}^i_\phi$ are orthogonal to the disclination dipole $\vec{\beta}_{ij}$ and symmetry implies that $\Sigma_i \vec{b}^i = 0$.

Since we shall only consider glide motion for which dislocations move in the ϕ direction, we may set $b^i_\theta = 0$. The elastic D-d interaction, Eq. (8), then reduces to

$$E_{Dd} \equiv \sum_{i=1}^{N_1} \sum_{j=1}^{N_2} \mathcal{E}_{Dd}(\beta_{ij}), \tag{10}$$

with

$$\mathcal{E}_{Dd}(\beta_{ij}) = -\frac{YR}{12} q_i b^j \left[\frac{\sin\beta_{ij} \ln\left(\frac{1-\cos\beta_{ij}}{2}\right)}{1+\cos\beta_{ij}} \right]. \tag{11}$$

The dislocation-dislocation interaction, Eq. (9), becomes

$$E_{dd} \equiv \sum_{i=1}^{N_2} \sum_{i>j}^{N_2} \mathcal{E}_{dd}(\beta_{ij}), \tag{12}$$

where

$$\mathcal{E}_{dd}(\beta_{ij}) = \frac{Y}{4\pi} b^i b^j \left[-\frac{\ln\left(\frac{1-\cos\beta_{ij}}{2}\right)}{1+\cos\beta_{ij}} - 1 \right]. \tag{13}$$

From now on we confine ourselves to the interaction between defects in a single scar and ignore the effects of the neighboring scars. In Fig. 5 we plot $\mathcal{E}_{Dd}$ (solid line) and $\mathcal{E}_{dd}$ (dotted line) as a function of the angular separation β, in units of Ya^2. Note that the disclination-dislocation interaction is attractive (for sufficiently short angular distance) while the dislocation-dislocation interaction is repulsive. The formation of grain boundary scars may now be understood as arising from the competition between the attractive binding

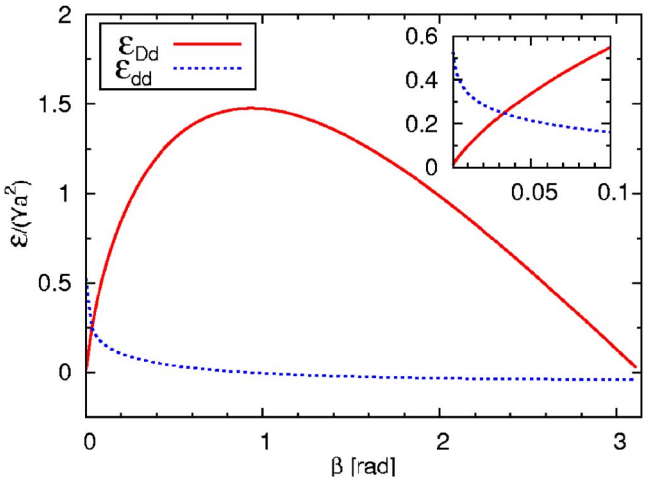

FIG. 5. (Color online) The disclination-dislocation (D-d) and dislocation-dislocation (d-d) interaction energies as a function of defect separation β. The inset is a blowup of the short-distance region of the plot.

of a dislocation to an excess disclination (D-d interaction) and the mutual repulsion between dislocations (d-d interaction). Figure 6 shows the D-d interaction energy as a function of angular distance for a variety of system sizes. The functional dependence of $\mathcal{E}_{Dd}/(Ya^2)$ on R/a given by Eq. (11) implies that the strength of the short-distance attraction increases with system size. As a result the strong D-d attraction for large systems leads to more excess dislocations within a scar to stabilize geometric frustration. Note that the crossover from an attractive to a repulsive interaction occurs at a universal value of the order of 1 rad, consistent with the predictions of Refs. [1,3].

The potential energy E_s of a single scar can be now obtained directly from the finite sum of pair interactions between defects:

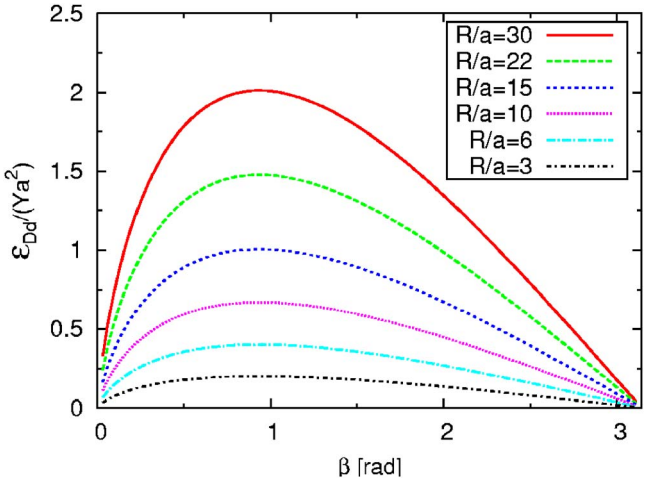

FIG. 6. (Color online) The disclination-dislocation (D-d) interaction energy versus angular separation β for a variety of system sizes.

$$E_s = \sum_i \mathcal{E}_{Dd}(\beta_i) + \sum_{i>j} \mathcal{E}_{dd}(\beta_{ij}), \tag{14}$$

where β_i is the angular distance of the ith dislocation from the center of the scar.

C. Dislocation elastic stiffness

We now compute the elastic stiffness [the spring constant in Eq. (1)] of dislocations within a scar. For that purpose, we consider small fluctuations of dislocations. Let us consider now small fluctuations of dislocations around their equilibrium positions in a scar with a fixed central disclination. The geodesic displacement of the ith dislocations will be denoted by s_i. We assume that the ith dislocation glides along the direction defined by the geodesic that starts at a point θ_{d_i} and forms an angle of $\pi/2$ with respect to the arc connecting θ_{d_i} to the other defect location under consideration (the disclination θ_D or the jth dislocations θ_{d_j}). The deformed geodesic arc distances $\tilde{\beta}$ will then be

$$\beta_i\colon D(\theta_D,0) \quad d_i(\theta_{d_i},0) \Rightarrow \tilde{\beta}_i\colon D(\theta_D,0) \quad d_i(\theta_{d_i},s_i/R),$$

$$\beta_{ij}\colon d_i(\theta_{d_i},0) \quad d_j(\theta_{d_j},0) \Rightarrow \tilde{\beta}_{ij}\colon d_i(\theta_{d_i},s_i/R) \quad d_j(\theta_{d_j},s_j/R), \tag{15}$$

where θ_D, θ_{d_i}, and θ_{d_j} are the initial locations of the disclination and the ith and jth dislocations, respectively, and $s_i, s_j \ll 0$. For an arbitrary scar along a meridian, the relation between β and $\tilde{\beta}$ is given by

$$\cos\tilde{\beta}_i = \cos\beta_i \cos(s_i/R),$$

$$\cos\tilde{\beta}_{ij} = \cos\beta_{ij} \cos[(s_i - s_j)/R]. \tag{16}$$

Expanding to second order gives

$$\tilde{E}_s = \tilde{E}_s|_{(0,0)} + \left[\left.\frac{\partial\tilde{E}_s}{\partial s_i}\right|_{(0,0)} s_i + \left.\frac{\partial\tilde{E}_s}{\partial s_j}\right|_{(0,0)} s_j \right] + \frac{1}{2}\left[\left.\frac{\partial^2\tilde{E}_s}{\partial s_i^2}\right|_{(0,0)} s_i^2 + 2 \left.\frac{\partial^2\tilde{E}_s}{\partial s_i \partial s_j}\right|_{(0,0)} s_i s_j + \left.\frac{\partial^2\tilde{E}_s}{\partial s_j^2}\right|_{(0,0)} s_j^2 \right]. \tag{17}$$

The first derivatives are easily seen to vanish, confirming that the initial configuration (linear and central symmetric) is a local minima:

$$\left.\frac{\partial\tilde{E}_s}{\partial s_i}\right|_{(0,0)} = \left.\frac{\partial\tilde{E}_s}{\partial s_j}\right|_{(0,0)} = 0. \tag{18}$$

The second derivatives are given by

$$\left.\frac{\partial^2 \tilde{E}_s}{\partial s_i^2}\right|_{(0,0)} = \sum \left(\frac{\partial \tilde{\mathcal{E}}_{Dd}}{\partial \cos \tilde{\beta}_i}\right)\left(\frac{\partial^2 \cos \tilde{\beta}_i}{\partial s_i^2}\right)\Bigg|_{(0,0)} + \sum \left(\frac{\partial \tilde{\mathcal{E}}_{Dd}}{\partial \cos \tilde{\beta}_{ij}}\right)\left(\frac{\partial^2 \cos \tilde{\beta}_{ij}}{\partial s_{ij}^2}\right)\Bigg|_{(0,0)}$$

$$\left.\frac{\partial^2 \tilde{E}_s}{\partial s_j^2}\right|_{(0,0)} = \sum \left(\frac{\partial \tilde{\mathcal{E}}_{Dd}}{\partial \cos \tilde{\beta}_{ij}}\right)\left(\frac{\partial^2 \cos \tilde{\beta}_{ij}}{\partial s_j^2}\right)\Bigg|_{(0,0)}$$

$$\left.\frac{\partial^2 \tilde{E}_s}{\partial s_i \partial s_j}\right|_{(0,0)} = \sum \left(\frac{\partial \tilde{\mathcal{E}}_{Dd}}{\partial \cos \tilde{\beta}_{ij}}\right)\left(\frac{\partial^2 \cos \tilde{\beta}_{ij}}{\partial s_i \partial s_j}\right)\Bigg|_{(0,0)}. \tag{19}$$

Equation (17) can then be written in terms of effective spring as

$$\Delta E_s = \frac{1}{2}\sum_i K_i s_i^2 + \frac{1}{2}\sum_{i>j} K_{ij}(s_i - s_j)^2, \tag{20}$$

where

$$K_i = \frac{Ya}{12R}\left[-\frac{1}{\sin \beta_i} - \frac{\ln\left(\frac{1-\cos\beta_i}{2}\right)}{\sin\beta_i(1+\cos\beta_i)}\right]\cos\beta_i \tag{21}$$

and

$$K_{ij} = \frac{Ya^2}{4\pi R^2}\left[-\frac{1}{\sin^2 \beta_{ij}} - \frac{\ln\left(\frac{1-\cos\beta_{ij}}{2}\right)}{(1+\cos\beta_{ij})^2}\right]\cos\beta_{ij}, \tag{22}$$

with β_i and β_{ij} determined by the initial configuration to be

$$\beta_i = |\theta_D - \theta_{d_i}|,$$

$$\beta_{ij} = |\theta_{d_i} - \theta_{d_j}|. \tag{23}$$

We note that the expressions for K_i and K_{ij} show singularities at $\beta = 0, \pi$. Those singularities are not real, as the validity of the above expressions is limited to $\beta > (a/R)$. Although expressions that correctly capture the $\beta \to 0$ limit may be derived, they are not necessary for the subsequent analysis.

We note that the deformation energy in Eq. (20) contains nondiagonal terms induced by the dislocation-dislocation interactions. The two stiffness coefficients K_i and K_{ij} result from D-d attractions ($\mathcal{E}_{dd}$) and d-d repulsions ($\mathcal{E}_{dd}$), respectively, which implies that $K_i > 0$ and $K_{ij} < 0$ for sufficiently short angular distance—i.e., $(a/R) < \beta < 1$ rad. Summing up we may write the energy shift as a general quadratic polynomial.

$$\Delta E_s = \frac{1}{2}\sum_{ij} \mathcal{K}_{ij} s_i s_j, \tag{24}$$

with $\mathcal{K}_{ij}$ given by

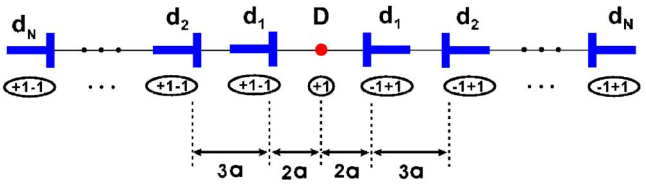

FIG. 7. (Color online) Dislocation spacings for a linear symmetric scar as highlighted within the blue box in Fig. 1.

$$\mathcal{K}_{ij} = \begin{cases} K_i + \sum_{i>k} K_{ik} & \text{if } i = j, \\ -2K_{ij} & \text{if } i > j. \end{cases} \tag{25}$$

For a pinned, small-angle grain boundary in flat space, the restoring force to shear stress has been obtained in Ref. [22], where it results from dislocation-dislocation interactions alone. The presence of disclination-dislocation interactions is a special feature of the two-dimensional curvature of the crystal. The eigenvalues k_i of the matrix $\mathcal{K}$,

$$\mathcal{K}V = k_i V, \tag{26}$$

give the effective stiffness coefficients with negative values, indicating that the associated dislocation will not bind to an equilibrium scar.

III. COMPARISON TO EXPERIMENT

We now use the formulas developed in the previous section to compute the elastic stiffness. The elastic stiffness depends on the particular configuration of dislocations. We compare our results with the experimental data given in Ref. [12]. The stiffness coefficients will depend on the detailed defect spacings in the ground-state configurations as well as the total number of excess dislocations in a scar. We assume that dislocations are equally spaced, as actually observed experimentally (see Fig. 2), although theoretical calculations predict that the spacing should grow with distance from the center of the scar [2,4]. We take the first dislocation be a distance $2a$ from the central disclination with the remaining dislocations spaced a distance $3a$ apart, as shown in Fig. 7.

For the numerical spring constants, we use the experimentally measured [12] two-dimensional Young's modulus $Y = 167 k_B T/a^2$. Note that the units of k_i and Y are all $k_B T/a^2$.

Spring constants for typical experimental sizes are plotted in Fig. 8. We see clearly that the elastic stiffness falls quickly as a function of distance from the central disclination, in agreement with general experimental results. At a quantitative level, the predicted values for the elastic stiffness, in unit of $k_B T/a^2$, are compared to the experimental quoted results of Ref. [12] in Table I. The continuum model predicts a very large value for the stiffness of the dislocation closest to the central disclination, and indeed, this dislocation appeared immobile in the experiments in Ref. [12], and no elastic stiffness could be measured. The results for the next dislocations are in very good agreement, more so given that the experiment only contains a single scar realization, and the theoretical calculations ignore interactions among scars or the coupling of dislocations to the underlying lattice.

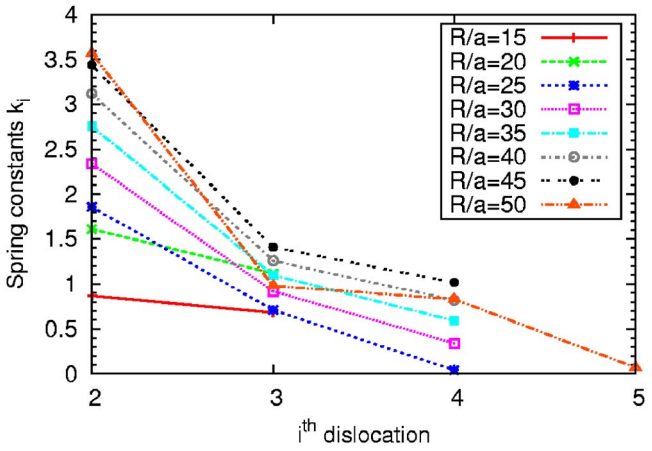

FIG. 8. (Color online) Spring constants k_i for each dislocation d_i, calculated for the configuration shown in Fig. 7.

IV. DYNAMICS OF VACANCIES AND INTERSTITIALS IN SPHERICAL CRYSTALS

We now analyze the dynamics of interstitials and vacancies. In Ref. [16], three types of vacancies V_{2a} (crushed vacancy), SV (split vacancy), and V_3 (threefold symmetric vacancy) were identified together with three interstitials I_3 (threefold symmetric interstitial), I_2 (twofold symmetric interstitial), and I_{2d} (disjoint twofold symmetric interstital). The I_3 interstitial and V_3 were found to be the most stable. Subsequent experiments [17] showed that the different interstitials and vacancies exist as stable defects, and their dynamics has recently been studied [18]. This situation is in contrast with spherical crystals where, to our knowledge, no interstitials or vacancies have been observed.

In order to investigate vacancies and interstitials we consider a system of 972 particles interacting with a Coulomb potential. In the initial configuration, there are only 12 disclination defects with the symmetry of the icosahedron, as shown in Fig. 9 (stage 0); this is an (8,3) icosadeltahedral configuration. We now force an I_2 interstitial by adding a particle, as shown in Fig. 9 (stage 1). I_2 evolves into I_3, the bound complex of dislocations with zero net Burgers vector (stage 2). It is found that the I_3 interstitial is unstable and starts to be ripped apart into three dislocations (stages 3 and 4) and eventually becomes three separate dislocations which each glide toward a fivefold disclination (stages 5 and 6). They quickly form a miniscar (a 5-7-5 grain boundary) at each of the vertices $5s$ by joining the nearest disclinations (stage 7). Snapshots of the dynamical sequence discussed above are shown in Fig. 9.

TABLE I. Comparison of the numerical spring constants (in units of K_BT/a^2), for individual dislocations, with the experimental values [12].

	R/a	k_1	k_2	k_3	k_4	k_5
Expt.	22	N/A	1.70	1.30	1.10	
Theory	22	12.78	1.86	1.28		
	26	13.78	1.96	0.75	0.11	
	32	15.20	2.52	1.00	0.44	
	50	18.19	3.57	0.98	0.83	0.07

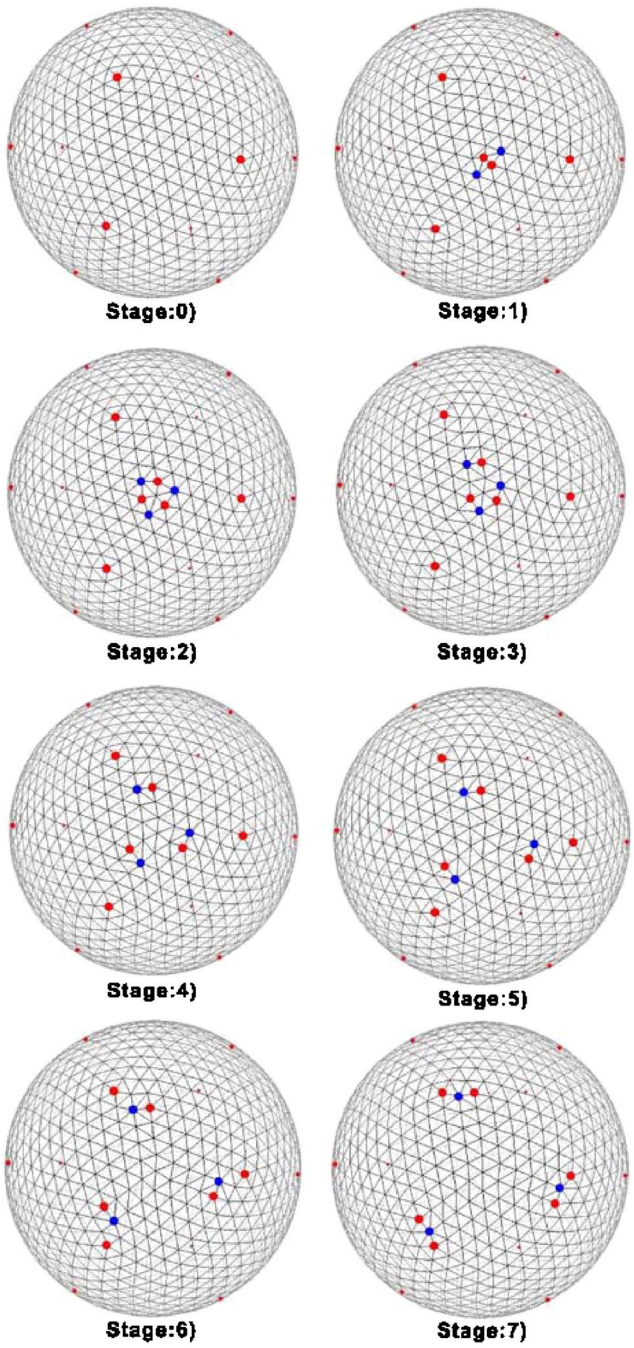

FIG. 9. (Color online) We first consider an initial lattice with icosahedron symmetry, an (8,3) icosadeltahedral lattice (stage 0). The I_2 interstitial is generated by adding one extra particle (stage 1), which evolves into a I_3 interstitial (stage 2). The curvature-driven unbinding of dislocations starts—the decay of an interstitial (stages 3 and 4). Individual dislocation glides towards the nearest isolated disclination (stages 5 and 6). Each dislocation binds to a disclination to form three miniscars (stage 7). The results are obtained from the java applet developed in Ref. [23], according to the procedure described in the Appendix.

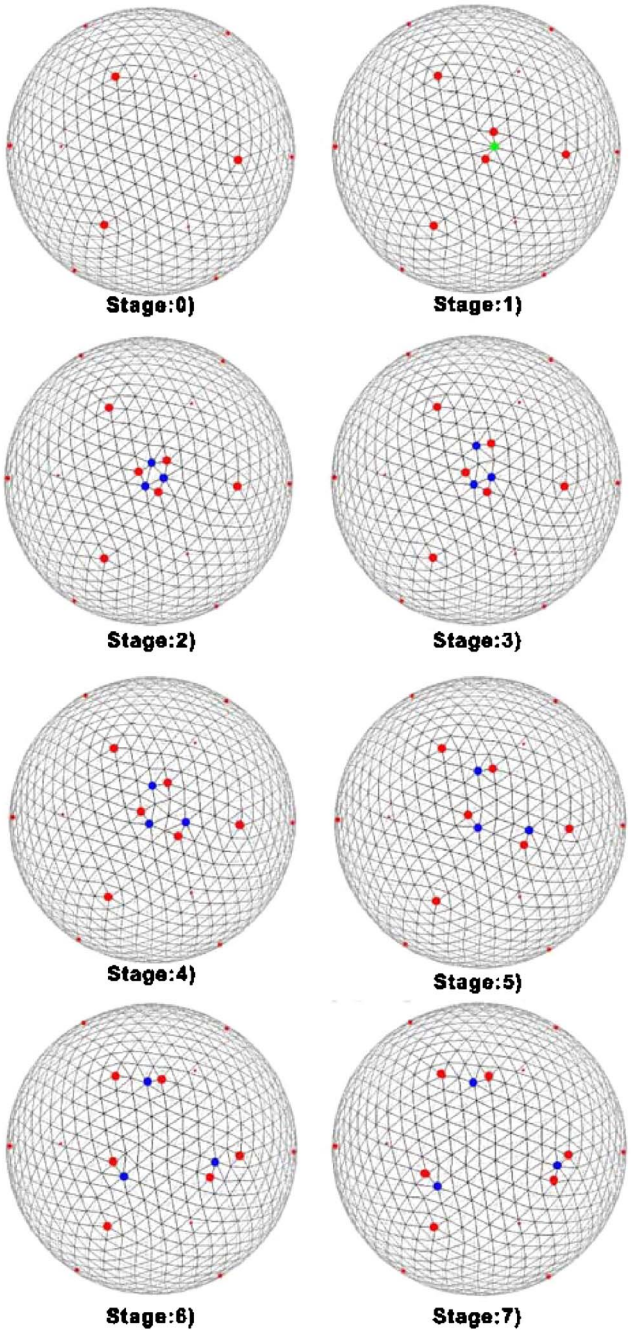

FIG. 10. (Color online) We first consider an initial lattice with icosahedron symmetry, an (8,3) icosadeltahedral lattice (stage 0). The *SV* vacancy is generated by subtracting one particle (stage 1), which evolves into a S_3 vacancy (stage 2). The curvature driven unbinding of dislocations starts—the decay of an vacancy (stages 3 and 4). Individual dislocation glides towards the nearest isolated disclination (stages 5 and 6). Each dislocation binds to a disclination to form three miniscars (stage 7). The results are obtained from the java applet developed in Ref. [23], according to the procedure described in the Appendix.

A similar analysis may be done for vacancies. By subtracting a particle from the initial icosadeltahedral configuration (8,3) in Fig. 10, the lattice develops the structurally unstable *SV* vacancy (stage 1), which subsequently evolves into V_3 (stage 2). Due to the energetic instability, V_3 eventually forms three scars via curvature driven unbinding (stages 3–7), similar to the interstitial.

TABLE II. Angular distance between defects during the relaxation of the interstitial shown in Fig. 9.

Stage	β_{d1D1}	β_{d1D2}	β_{d1D3}	β_{d1d2}	β_{d1d3}
2	0.5954	0.7379	0.6796	0.1222	0.1222
3	0.4402	0.8379	0.7335	0.2116	0.2445
4	0.3231	0.9420	0.8003	0.4224	0.4402
5	0.3231	0.9420	0.8003	0.5594	0.5594
6	0.2116	1.0488	0.8767	0.7379	0.7379
7	0.1222	1.0739	0.9601	0.9420	0.9420

Similar results also follow by considering 972 particles interacting with a general potential $1/r^{\gamma}$ (the generalized Thomson problem), thus showing that the instabilities of vacancies and interstitials are a universal feature of two-dimensional spherical crystals.

The instabilities of vacancies and interstitials are predicted from the continuum elastic model described in this paper. To apply Eq. (14) we first need to estimate the angular distances between defects at each stage. An (8,3) icosadeltahedral lattice, with $M=972$ particles, corresponds to system size $R/a \approx 8.2$ [using $M \approx \frac{8\pi}{\sqrt{3}}\left(\frac{R}{a}\right)^2$]. The relevant angular distances between defects can then all be calculated by simple counting together with spherical trigonometry. The results so obtained are shown in Table II. Taking the orientation of the Burgers vectors appropriately into account we may then compute the total interaction energy at each stage using Eq. (14). The evolution of the total energy is shown in Fig. 11. The energy monotonically decreases until the final *scarred* state is reached.

V. CONCLUSIONS

In this paper we have studied the dynamics of point defects in two-dimensional spherical crystals. Our results pro-

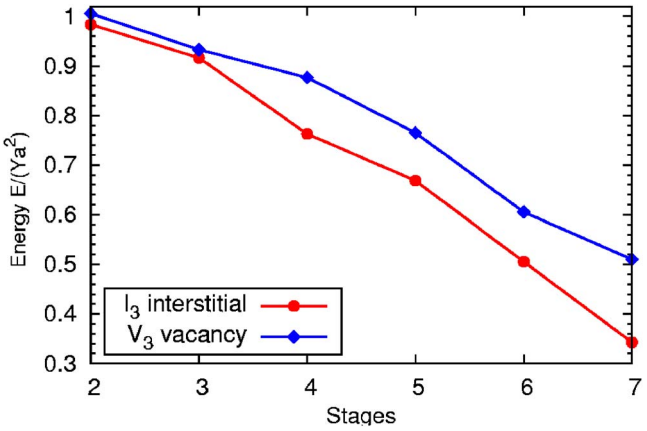

FIG. 11. (Color online) Continuum elastic energy from Eq. (14) for the configurations in Figs. 9 and 10. The initial configuration is an I_3 interstitial or a V_3 vacancy, both of which are unstable to scar formation. The small difference in elastic energy for both I_3 and V_3 results from different final configurations (see Figs. 9 and 10).

vide explicit predictions for the dislocation elastic stiffness that compare quite favorably with experimental data. We also analyzed the dynamics of interstitials and vacancies and found that the effects of curvature are quite dramatic, as defects that are stable in flat space become unstable in curved space.

A number of issues raised in this paper will require further investigations. The process of generating vacancies and interstitials can be repeated indefinitely. It should be expected that in this way, we can grow longer scars, whose length should saturate at some point. What structures follow will be the subject of further investigations. Although our presentation has focused on the sphere, the results should apply equally to other geometries. It is expected that in arbitrary geometries, vacancies or interstitials should become unstable to the formation of scars nucleated by existing disclinations.

Detailed experimental verification of our results could be achieved from experiments of colloids absorbed on oil-water interface as in Refs. [10,12]. Using holographical optical tweezers [17] applied to a spherical crystal, it should be possible to remove one colloid, thus creating a vacancy, which according to the results in our paper would become unstable and join existing scars, which could be visualized as described in Ref. [12]. More rigorous validations for the predictions in this paper can be accomplished by a more comprehensive analysis of experimental data such as the one presented in Ref. [12].

In summary, the results presented in this paper show the dramatic effects of curvature in two-dimensional crystals. It is our expectation that this paper will motivate further experimental and computational work.

ACKNOWLEDGMENTS

We would like to thank David Nelson for discussions. The work of Mark Bowick and Homin Shin was supported by the NSF through Grant No. DMR-0219292 (ITR) and through funds provided by Syracuse University. The work of A.T. was supported by the NSF through Grant No. ITR-DMR-0426597 and partially supported by the DOE through Ames Lab under Contract No. W-7405-ENG-82.

APPENDIX: ANALYSIS OF VACANCIES AND INTERSTITIALS USING THE JAVA APPLET

The analysis of the stability of vacancies and interstitials (see Figs. 9 and 10) has been obtained using the java applet available at Ref. [23]. In order to reproduce the results, we generate a (8,3) icosadeltahedral tessellation using the construct (m,n) algorithm with $m=8$ and n. Now add or remove a single particle to the lattice at the barycenter of a spherical triangle whose vertices are three nearest-neighbor five-fold disclinations by (shift+click) or (Ctrl+click). The *self-interstitial* (or *self-vacancy*) so formed is then relaxed by a standard relaxation algorithm. One immediately finds that a V_2 interstitial (or a *SV* vacancy) is structurally unstable. In a few time steps it morphs into a complex of dislocations with zero net Burgers vector—the most common structure observed is a set of three dislocations (I_3 or V_3) arranged in a hexagon. Removing a particle (or adding a particle) back restores the particle number to the original 972 and relaxing still leaves scars with total energy lower than the starting configuration with 12 isolated 5's. This establishes that scars are definitely low-energy equilibrium states rather than artifacts of the relaxation algorithm.

[1] M. J. Bowick, D. R. Nelson, and A. Travesset, Phys. Rev. B **62**, 8738 (2000).
[2] M. Bowick, A. Cacciuto, D. R. Nelson, and A. Travesset, Phys. Rev. Lett. **89**, 185502 (2002).
[3] M. J. Bowick, A. Cacciuto, D. R. Nelson, and A. Travesset, Phys. Rev. B **73**, 024115 (2006).
[4] A. Travesset, Phys. Rev. E **72**, 036110 (2005).
[5] A. Perez-Garrido, M. J. W. Dodgson, and M. A. Moore, Phys. Rev. B **56**, 3640 (1997).
[6] V. N. Manoharan, Solid State Commun. **139**, 557 (2006).
[7] M. Bowick, D. R. Nelson, and A. Travesset, Phys. Rev. E **69**, 041102 (2004).
[8] V. Vitelli and D. R. Nelson, Phys. Rev. E **70**, 051105 (2004).
[9] V. Vitelli, J. B. Lucks, and D. R. Nelson, Proc. Natl. Acad. Sci. U.S.A. **103**, 12323 (2006).
[10] A. Bausch *et al.*, Science **299**, 1716 (2003).
[11] T. Einert, P. Lipowski, J. Schilling, M. Bowick, and A. R. Bausch, Langmuir **21**, 12076 (2005).
[12] P. Lipowsky, M. J. Bowick, J. H. Meinke, D. N. Nelson, and A. R. Bausch, Nat. Mater. **4**, 407 (2005).
[13] X. S. Ling, Nat. Mater. **4**, 360 (2005).
[14] D. S. Fisher, B. I. Halperin, and R. Morf, Phys. Rev. B **20**, 4692 (1979).
[15] R. L. Blumberg Selinger, Z-G. Wang, and W. Gelbart, J. Chem. Phys. **95**, 9128 (1991).
[16] S. Jain and D. R. Nelson, Phys. Rev. E **61**, 1599 (2000).
[17] A. Pertsinidis and X. S. Ling, Nature (London) **413**, 147 (2001); Phys. Rev. Lett. **87**, 098303 (2001); New J. Phys. **7**, 33 (2005).
[18] A. Libal, C. Reichhardt, and C. J. Olson Reichhardt, Phys. Rev. E **75**, 011403 (2007).
[19] E. L. Altschuler and A. Perez-Garrido, Phys. Rev. E **71**, 047703 (2005).
[20] S. Xiao and W. Hou, Phys. Rev. B **73**, 115406 (2006).
[21] R. Peierls, Proc. Phys. Soc. London **52**, 34 (1940).
[22] R. Bruinsma, B. I. Halperin, and A. Zippelius, Phys. Rev. B **25**, 579 (1982).
[23] M. Bowick, C. Cecka, and A. Middleton, http://physics.syr.edu/condensedmatter/thomson/.